

Observation of Negative Refraction and Focusing in Two-Dimensional Photonic Crystals

To cite this article: Ekmel Ozbay *et al* 2006 *Jpn. J. Appl. Phys.* **45** 6064

View the [article online](#) for updates and enhancements.

Related content

- [Imaging by photonic crystal without negative refraction](#)
Y Fang
- [Frequency bands of negative refraction infinite one-dimensional photonic crystals](#)
Chen Yuan-Yuan, Huang Zhao-Ming, Shi Jie-Long *et al.*
- [Imaging by Photonic Crystal Using Reflection and Negative Refraction](#)
Fang Yun-Tuan and Sun Hai-Jin

Recent citations

- [Realization of Negative Refraction in a Bifilar Prism-Type Array Metamaterial](#)
Alexei Balmakou *et al*

Invited Paper

Observation of Negative Refraction and Focusing in Two-Dimensional Photonic Crystals

Ekmel OZBAY^{1,2,3*}, Irfan BULU^{1,2}, Kaan GUVEN^{1,2}, Humeyra CAGLAYAN^{1,2} and Koray AYDIN^{1,2}

¹Nanotechnology Research Center, Bilkent University, Bilkent, Ankara 06800, Turkey

²Department of Physics, Bilkent University, Bilkent, Ankara 06800, Turkey

³Department of Electrical and Electronics Engineering, Bilkent University, Bilkent, Ankara 06800, Turkey

(Received February 6, 2006; accepted May 2, 2006; published online August 4, 2006)

We experimentally and theoretically demonstrate the negative refraction and focusing of electromagnetic (EM) waves by two-dimensional photonic crystal slabs at microwave frequencies. The negative refraction is observed both for transverse magnetic (TM) and transverse electric (TE) polarized incident EM waves. Gaussian beam shifting method is used to verify the negative refractive index. The subwavelength imaging and flat lens behavior of photonic crystals are successfully demonstrated. We have been able to overcome the diffraction limit and focus the EM waves to a spot size of 0.21λ . Metallodielectric photonic crystals are employed to increase the range of angle of incidence that results in negative refraction. Experimental results and theoretical calculations are in good agreement throughout the work. [DOI: 10.1143/JJAP.45.6064]

KEYWORDS: Negative refraction, photonic crystals, photonic band gap, band diagram, equal frequency contours, flat lens, subwavelength imaging, metamaterial, left-handed materials

1. Introduction

Photonic crystals (PC) are periodic dielectric or metallic structures that have photonic bands exhibiting arbitrarily different dispersions for the propagation of electromagnetic waves, and band gaps, where the propagation is prohibited at certain range of wavelengths.^{1–3} From fundamental physics point of view, photonic crystals provide access to novel and unusual optical properties. It has been theoretically shown that photonic crystals may exhibit negative refraction although they have a periodically modulated positive permittivity and permeability of unity.^{4–7} Cubukcu *et al.* has been first to demonstrate negative refraction phenomenon in a two-dimensional (2D) PC in the microwave regime.⁸ Further experimental studies proved that carefully designed PCs are candidates for obtaining negative refraction at microwave⁹ and infrared¹⁰ frequency regimes. The super-prism effect is another exciting property arising from the photonic crystals.^{11,12} Subwavelength imaging and resolution¹³ and flat lens behavior¹⁴ of PCs have been experimentally demonstrated. Extensive numerical^{15–18} and experimental studies^{19–24} provided a better understanding of negative refraction, focusing and subwavelength imaging in photonic crystal structures. Negative refraction is also achievable by using artificially constructed left-handed materials (LHM).^{25–30} In such materials the mechanism for the negative refraction is quite different.^{31–34} For the LHM structures the effective permittivity and the permeability are simultaneously negative resulting in an effective negative refractive index. However for the PCs the band structure lead to negative dispersion for electromagnetic (EM) waves.^{35–39}

In this paper, we review recent studies on the negative refraction and focusing of electromagnetic waves by photonic crystal slabs in the microwave frequency regime. The paper is organized as follows: Sections 2 and 3 present the negative refraction and focusing of transverse magnetic (TM) and transverse electric (TE) polarized electromagnetic

waves, respectively, using two different 2D dielectric photonic crystals. In §4, we extend the study in the preceding sections to a metallodielectric PC. We found that the focusing abilities of a PC slab can surpass that of conventional (i.e., positive refractive) materials, providing both subwavelength imaging and true flat lens behavior.^{40–43}

2. Negative Refraction and Subwavelength Imaging of TM Polarized Electromagnetic Waves

The 2D photonic crystal structure that we use in our experiments, consists of a square array of dielectric rods in air, having a dielectric constant $\epsilon = 9.61$, radius $r = 1.6$ mm, and length $l = 150$ mm.⁸ The periodicity of the structure in both directions is $a = 4.79$ mm. The analysis of Luo *et al.*⁶ is followed to determine the negative refraction frequency range of our structure, which is calculated to be 13.10–15.44 GHz. Propagation properties of the EM wave within the crystal can be described by studying equal-frequency contours (EFCs) in k -space. The TM polarized band diagram of the photonic crystal calculated by plane wave expansion method, is shown in Fig. 1(a). We focus on the first band for the experimental and theoretical demonstration of single beam negative refraction in two dimensional photonic crystals. EFCs of the photonic crystal and air at 13.698 GHz are schematically

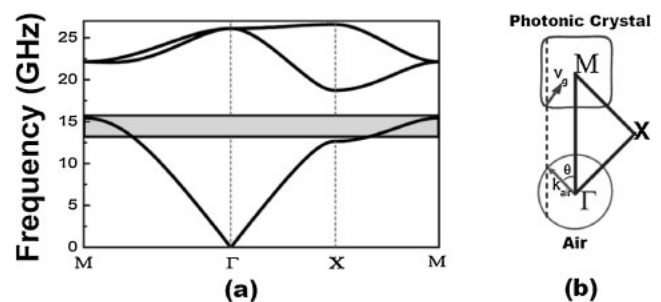


Fig. 1. (a) Calculated band diagram of 2D photonic crystal for transverse magnetic (TM) polarization. (b) Equal-frequency contours in k -space of PC and air at 13.698 GHz. θ is the incident angle and v_g is the group velocity inside the PC.

*E-mail address: ozbay@bilkent.edu.tr

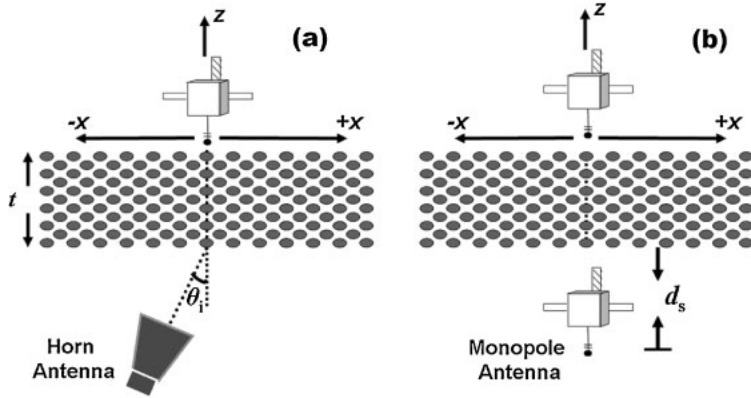


Fig. 2. Schematic drawing experimental setup for observing (a) negative refraction phenomenon, (b) focusing effect of a slab of negative refractive 2D PC.

drawn in Fig. 1(b). The conservation of the surface-parallel wave vector gives the direction of the refracted waves inside the PC.⁶⁾ The negative refraction effect is present at this frequency.

The refraction spectrum is measured by a setup consisting of an HP 8510C network analyzer, a standard high gain microwave horn antenna as the transmitter, and a monopole antenna as the receiver [Fig. 2(a)]. The size of the monopole antenna is 11 mm, which is half of the operation wavelength ($\lambda \sim 22$ mm) of the EM wave at a working frequency of $f = 13.698$ GHz. The top view of the experimental setup is given in Fig. 2(a), the x and z directions are shown in the figure, whereas the y is directed to the out of page. The electric field is along the y direction (i.e., parallel to the rods), whereas the magnetic field and wave-vector are on the x - z plane. The horn antenna is oriented such that the incident waves make an angle of 45° with the normal of ΓM interface.

The spatial distributions of the time averaged incident field intensity along the second (PC-air) interface are measured [Fig. 3(a)]. The PC used in negative refraction experiments has 17 layer along the propagation direction (z) and 21 layers along the lateral direction (x). For a direct comparison of theoretical predictions and experimental results, simulation of the structure based on experimental parameters using a finite difference time domain (FDTD) method is performed. The incident EM wave has a Gaussian beam profile centered at $x = 0$. Therefore, by measuring the shift of the outgoing beam as given in Fig. 3(a), one can easily deduce whether the structure has a positive or negative refractive index.

Figure 3(b) plots the measured (solid) and simulated (dashed-dotted) spatial distributions of intensity at the interfaces for the slabs of PC (black) and polystyrene pellets (gray). As clearly seen in Fig. 3(b), the center of the outgoing Gaussian beam is shifted to the left side of the center of the incident Gaussian beam for the PC structure. Due to Snell's law, this behavior corresponds to negative refraction. Experimental results and numerical simulations agree well. Refractive index of PC at 13.698 GHz determined from the experiment is -1.94 , which is very close to the theoretical value of -2.06 computed by the FDTD method. For comparison purposes, the measurements and the simulations are repeated with a slab that contains only polystyrene pellets, which has a positive refractive index ($n = 1.46$). The refracted beam emerges from the right hand

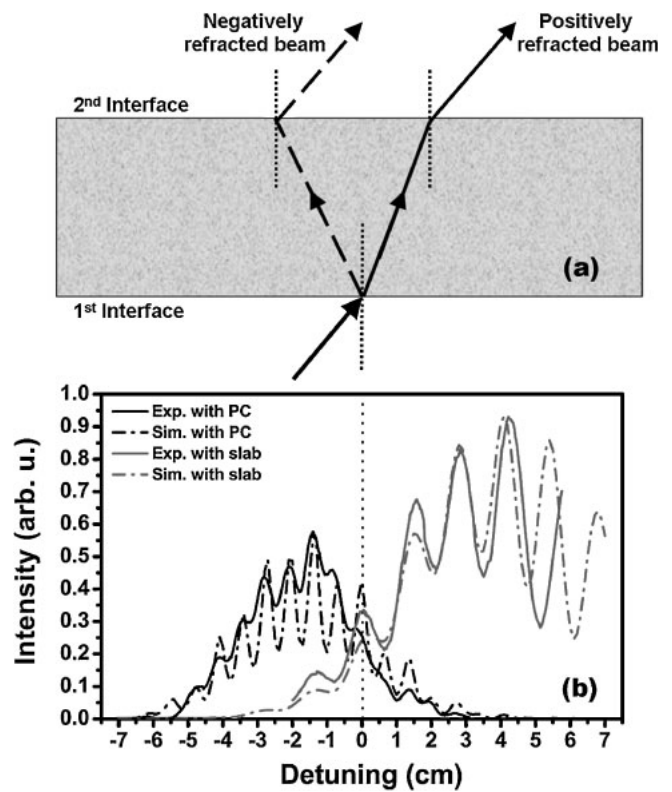


Fig. 3. (a) Schematics of refraction of incident beam through positive and negative media. (b) Refraction spectrum of incident beam through negative refractive PC (black lines) and positive refractive polystyrene pellets (gray lines). The solid lines and the dashed-dotted lines correspond to the experimental measurements and theoretical simulations, respectively.

side of the incident beam as plotted in Fig. 3(b). The positive refractive index determined from the experiment is 1.52, which is close to the tabulated value of 1.46.

A negative refractive index allows a flat lens to bring EM waves into focus, whereas positive refractive index materials always require curved surfaces to focus EM waves.^{25,27)} One interesting physical behavior of negative index materials is that they can restore the amplitude of evanescent waves and therefore enable subwavelength focusing.^{15,27)} Subwavelength resolution was experimentally verified for negative index materials made of PCs.⁸⁾ To investigate the focusing ability of the present PC, a slab of same PC (with 15×21 layers) is employed. The operation frequency is set to

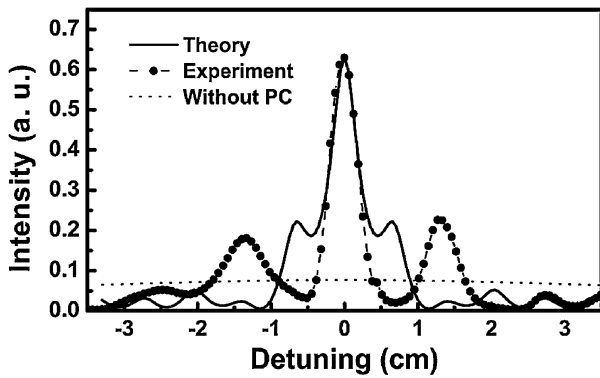


Fig. 4. Measured power distribution (—●—) and calculated average intensity (solid line) at the focal point. Dashed line is the spatial power distribution without PC.

13.698 GHz, having the largest angular range for negative refraction.⁸⁾ FDTD simulations with experimental parameters predict the formation of an image 0.7 mm away from the PC–air interface for a point source that is placed 0.7 mm away from the air–PC interface. We first simulated the distribution of time-averaged intensity along the PC–air interface with and without the PC (solid curve and thin dotted curve in Fig. 5). In the experiment, a monopole antenna is used as the point source [Fig. 2(b)]. The measured (solid) and calculated (large dotted-dashed) power distribution along the interface is depicted in Fig. 4. The full width at half maximum (FWHM) of the measured focused beam is found to be 0.21λ , which is in good agreement with the calculated FWHM. In contrast, the calculated FWHM of the beam at this plane in the absence of the PC is found to be 5.94λ (dashed line in Fig. 4). This implies an enhancement of the transmitted field about 25 times compared to that of free space.

3. Negative Refraction and Point Focusing of TE Polarized Electromagnetic Waves

In the previous section the negative refraction originating from the convex EFCs of the first band around the M -point in k -space is investigated. The first band has a partial gap around Γ -point, and the EM waves are forced to move along the ΓM direction, where the conservation of the surface-parallel component of the wave vector causes negative refraction [Fig. 1(a)]. In this section, we employ a different band topology of a 2D PC to obtain negative refraction.¹⁹⁾ We aim to achieve negative refractive index with higher isotropy. Based on the analysis presented in ref. 17, we utilize a TE polarized upper band of the PC where the

magnetic field is parallel to the dielectric rods. A similar study using TM polarized band was recently reported by Martinez *et al.*²¹⁾

Figure 5(a) depicts the calculated band diagram in the first Brillouin zone. The transverse direction is taken to be in the plane of 2D PC. We scaled frequency with $\tilde{f} = f(a/c)$. The fifth band as shaded in the Fig. 5(a) extends from $\tilde{f} = 0.65$ ($f = 40.65$ GHz) to $\tilde{f} = 0.74$ ($f = 46.27$ GHz). Figure 5(b) plots the EFCs in the full Brillouin zone. The EFCs of the band shrink with increasing frequency, contrary to the EFCs in air ($n = 1$).

The refraction spectra are measured by using same setup as in Fig. 2(a). Since the EM wave is TE polarized in this case, the horn and the monopole antennas are rotated by 90° degrees. Therefore the magnetic field is parallel to the dielectric rods. The PC structure consists of seven layers along the propagation direction (z) and 31 layers along the lateral direction (x). The horn antenna is on the negative side of the PC with respect to its central axis. The scanning is performed along the second PC–air interface by $\Delta x = 1.27$ mm steps. The refraction spectra of the EM waves for three different incident angles are measured and the results are plotted in Fig. 6. The top part of Fig. 6 shows the field distribution along the PC–air interface as a function of

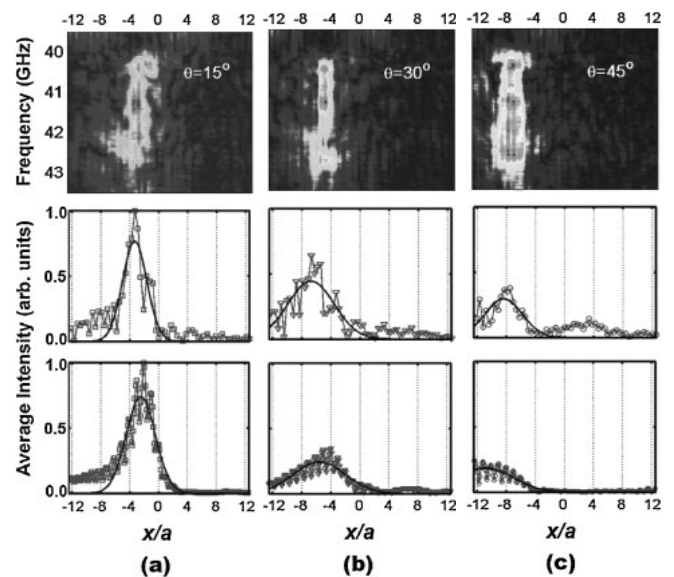


Fig. 6. Measured refraction spectra of the fifth band along the PC–air interface for incidence angles of (a) $\theta_i = 15^\circ$, (b) $\theta_i = 30^\circ$, and (c) $\theta_i = 45^\circ$ is given on the top figures. Middle figures are the measured, whereas the bottom figures are the simulated intensity profiles at 41.7 GHz for the respective angles of incidence. Solid curves indicate the Gaussian fits of the data.

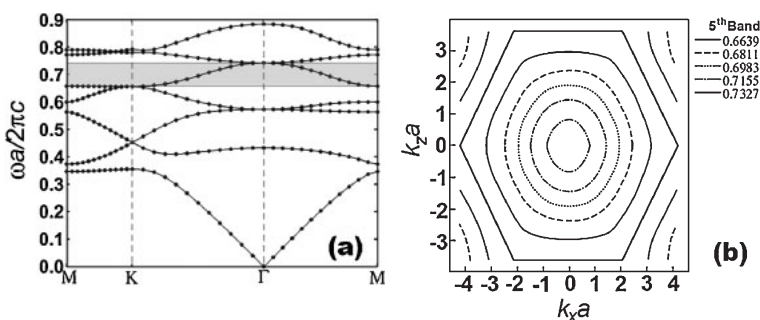


Fig. 5. (a) Calculated TE polarized band structure. Shaded band (fifth band) covers the frequencies where the structure possess negative index of refraction. (b) Equal-frequency contours of the fifth band in the full Brillouin zone. The contours are nearly circular (i.e. isotropic) and shrink with increasing frequency.

frequency. It is evident that the refracted beam appears for the angle of incidence (a) $\theta_i = 15^\circ$, (b) $\theta_i = 30^\circ$, and (c) $\theta_i = 45^\circ$ on the negative side, indicating that the PC structure has negative refractive index between 40.0–43.0 GHz.

When the incidence angle is increased, the transmission shifts to the left accordingly. In order to investigate the beam profiles, the spatial cross sections at $f = 41.7$ GHz are plotted in the middle part of Fig. 6. The intensities are normalized with respect to the maximum intensity for the incident angle $\theta_i = 15^\circ$. It is apparent that the lateral shift is accompanied by a decrease in the transmission intensity. This is mainly due to the higher reflection at the interface for larger incidence angles. The diffraction-induced out-of-plane loss which occurs during the propagation through the PC also contributes to the decrease in intensity. The bottom part of Fig. 6 displays the simulated average field intensity at $f = 41.7$ GHz. Experimental results agree well with the FDTD simulations. By using Snell's law, index of refraction is obtained to be $n_{\text{eff}} = -0.52, -0.66,$ and -0.86 from the experiment for $\theta_i = 15, 30$ and 45° , respectively. The simulation results for the same incidence angles give $n_{\text{eff}} = -0.66, -0.72,$ and -0.80 . The experimental and theoretical results agree quite well.

We have also investigated the focusing properties of our PC slab for TE polarized EM waves. FDTD simulations are performed for a monopole source radiating at $f = 42.07$ GHz and located at a distance $d_s = 2\lambda$ away from air–PC interface. Figure 7(a) displays the resulting spatial intensity distribution in the image plane, normalized to the value of maximum intensity along the center ($x = 0$) of the beam. The PC–air interface is located at $z = 0$. The peak indicates focusing behavior unambiguously. We would like to emphasize that the focusing occurs away from the PC–air interface, observed at $z \approx 8\lambda$. Therefore, unlike the focusing discussed in previous section for TM polarized EM wave, this PC does not perform imaging. Also a subwavelength imaging as presented in Fig. 4 is not present since the focal point is quite far away from the interface.

Experimental setup for verifying the focusing through a slab of PC is similar to the one discussed in the previous section [Fig. 2(b)]. In this case, a waveguide aperture in TE polarization is used as an approximation to an omnidirectional source. The waveguide aperture provides sufficiently omni-directional radiation due to the diffraction at the aperture.¹⁹⁾ The intensity distribution in the focusing plane is measured by a monopole antenna. For $d_s = 2\lambda$, first, a scan

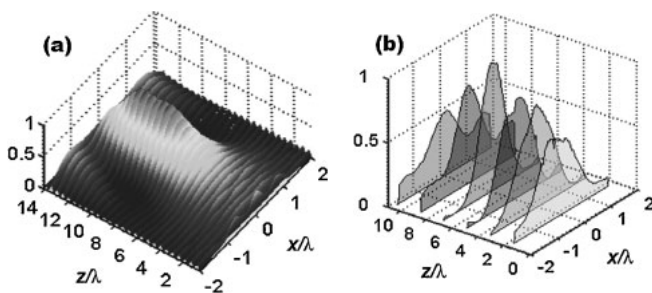


Fig. 7. (a) Simulated 2D intensity profile in the image plane. $z = 0$ corresponds to the PC–air interface. (b) Measured lateral intensity profiles along the propagation direction. Measurements are performed at six different positions $z/\lambda = 1.78, 3.56, 5.34, 7.12, 8.90,$ and 10.68 .

is performed along the propagation direction (z) to locate the maximum intensity, i.e., the focal point. Then, lateral cross sections (along x) of field intensity at several z points around the peak position are measured. As seen in Fig. 7(b), the beam is focused both in lateral and longitudinal directions. The maximum intensity is observed at $z \approx 8\lambda$, the focal point. The longitudinal extend of the focusing indicates that index of refraction deviates from negative unity, and bears a certain amount of anisotropy. We stress that even when refractive index was perfectly isotropic and uniform, a value different from $n = -1$ would not generate point focusing and would induce an aberration of the image.

4. Negative Refraction and Focusing Analysis for a Metallodielectric PC

In §2 and 3 we have dealt with dielectric photonic crystals. Photonic crystal structures can also be made of metals. But it is not easy to obtain negative refraction from the metallic photonic crystal structures since the EFCs of the metallic PCs are larger than the EFCs of air. Luo *et al.* theoretically demonstrated that it is indeed possible to obtain all-angle negative refraction by embedding metallic rods into a high-dielectric constant medium.¹⁶⁾ The main idea for using a medium with high dielectric permittivity is to increase the effective index of the photonic crystal. The advantage is that the EFCs will be lowered in frequency but the area occupied by EFCs in k space will not change. Following this basic idea, we used a different approach for constructing the PC structure. Instead of embedding metallic rods into a high-dielectric medium, we combined dielectric rods and metallic rods together to form a metallodielectric PC. Metallodielectric PC could be considered as a metallic PC with a periodic dielectric perturbation. Positive dielectric constant is an attractive perturbation and causes lowering the frequency of the bands.²²⁾

The metallodielectric photonic crystal is a square lattice of metallic and dielectric rods where the basis of the PC consists of a metallic and a dielectric rod placed along the diagonal of the square unit cell as given in the inset of Fig. 8(b). Cylindrical alumina rods with a radius of 1.55 mm are used as the dielectric rods with $\epsilon = 9.61$. The metallic

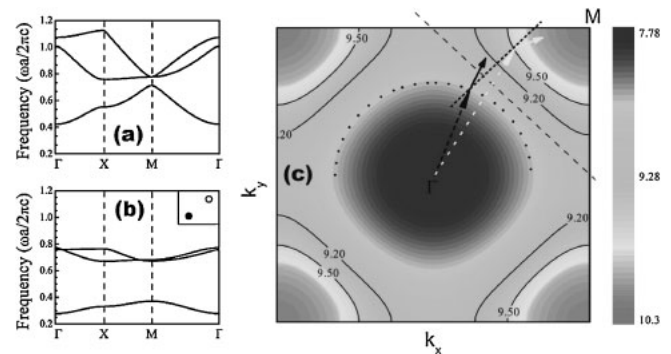


Fig. 8. (a) Calculated TM-polarized bands for the metallic photonic crystal, and (b) the metallodielectric crystal. (c) Equal-frequency contours (solid curves) are shown for the metallodielectric PC. Dotted circle is the free-space equal-frequency contour at 9.5 GHz. Free-space wave vector (black dashed arrow), free-space group velocity (black solid arrow), wave vector of the refracted waves in the PC (white dashed arrow), group velocity inside the PC (white solid arrow) are drawn.

rods are made of aluminum and have a radius of 1.5 mm. Both the metallic and dielectric rods have a height of 150 mm.

The band diagrams of metallic PC [Fig. 8(a)] and metalodielectric PC [Fig. 8(b)] are computed for TM polarized EM waves. The radius of the dielectric rod is $0.136a$, and the radius of the metallic rod is $0.14a$, where a is the lattice constant. Lattice constant is same in these structures. By comparing Figs. 8(a) and 8(b) we can conclude that the bands of the metalodielectric photonic crystal are lowered in frequency compared to the bands of the metallic photonic crystal.

Equal-frequency contours of the metalodielectric PC for TM polarization over the first Brillouin zone is plotted in Fig. 8(c). The dotted circle is the EFC of air. The PC surface is aligned such that the normal vector to the air-PC interface is along the ΓM direction. Since the surface-parallel component of the wave vector is conserved, the wave vectors of the refracted beam can easily be obtained, as given in the figure. The group velocity of the incident waves and the group velocity of the transmitted waves fall on opposite sides of the surface normal. Therefore the incident waves are negatively refracted.⁶⁾ For the plotted EFCs, the magnitude of the largest surface-parallel wave vector component in air is smaller than the largest surface-parallel wave vector component in the photonic crystal. In addition, the group velocities in free space and the group velocities in the photonic crystal fall on different sides of the surface normal. As a result, EM waves are negatively refracted for all incidence angles. The range of incidence angles that are negatively refracted can be increased by lowering the bands without modifying the lattice parameters.²²⁾

The electric field intensities are measured along the PC-air interface to demonstrate the negative refraction experimentally. The measurement method is same with the measurements indicated in the previous sections [Fig. 2(a)]. Waves that are positively refracted are expected to emerge from the positive side of the surface, whereas negatively refracted waves are to emerge from the negative side. Measurement results for incidence angles of $\theta_i = 15, 25, 35,$ and 45° are provided in Figs. 9(a), 9(b), 9(c), and 9(d), respectively. Between the frequencies 9.20 and 10.30 GHz waves exit from the negative side of the PC meaning that EM waves are negatively refracted by the PC at this frequency range. Upto 9.20 GHz the waves positively refracted.

We have also performed FDTD simulations to see how the EM wave is refracted by the metalodielectric PC. We have sent an incident Gaussian beam to the air-PC interface and calculated electric field intensities inside and outside the PC at 9.70 GHz. The simulation results for two different incident angles $\theta_i = 15^\circ$ [Fig. 10(a)] and $\theta_i = 45^\circ$ [Fig. 10(b)] clearly show that the negative refraction takes place at this frequency. The effect of reflection is also clear in this picture. For higher incident angle the intensity (therefore the transmission) is lower due to the high reflections from the air-PC interface. Note that 9.70 GHz is in the negative refraction frequency regime as calculated from the EFCs [Fig. 8(c)].

We have compared the experimental and theoretical results of the values of refractive indices at $\theta_i = 25^\circ$

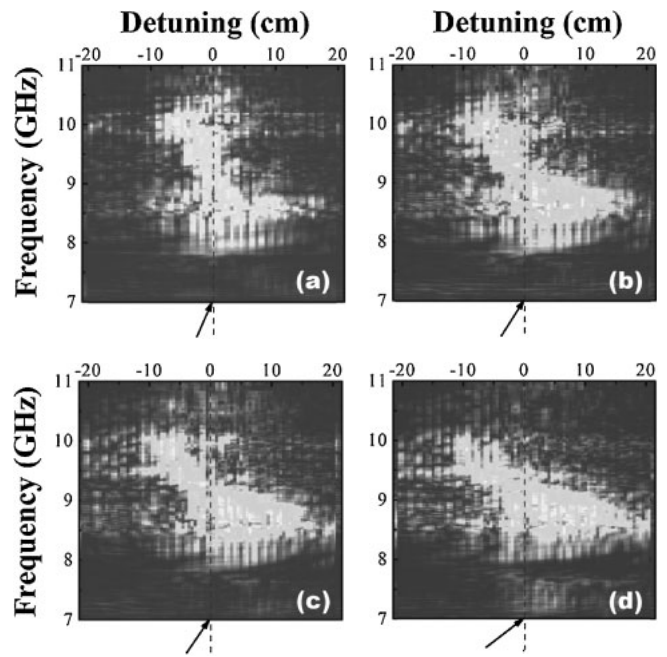


Fig. 9. Measured electric field intensities along the PC-air interface for incident angles of (a) $\theta = 15^\circ$, (b) $\theta = 25^\circ$, (c) $\theta = 35^\circ$, and (d) $\theta = 45^\circ$. The intensities are plotted as a function of frequency. Upto 9.2 GHz structure positively refracting, between 9.2 and 10.3 GHz structure refracts negatively.

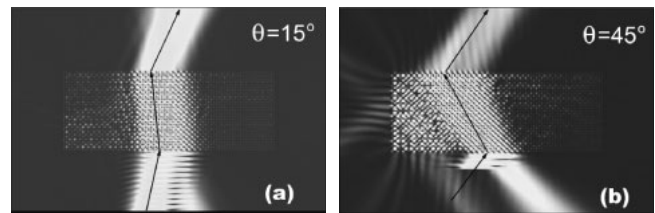


Fig. 10. Simulated electric field distributions for both angles of incidence. incident angles of (a) $\theta = 15^\circ$, and (b) $\theta = 45^\circ$. Negative refraction phenomenon is clearly observed for both angles of incidence.

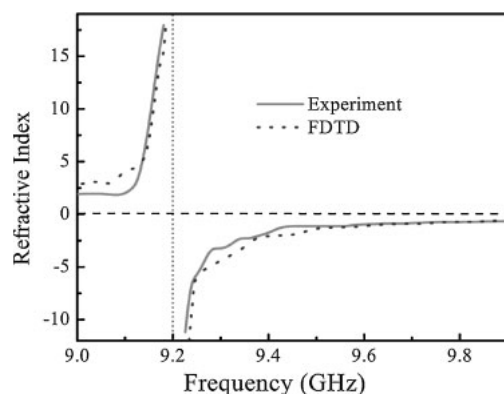


Fig. 11. Measured (solid line) and calculated (dashed line) refractive indices at an angle of incidence 15° .

incidence angle in Fig. 11. Between 9.00 and 9.19 GHz the refractive indices are found to be positive. Around 9.20 GHz there is an abrupt change at the values and the sign of the index of refraction. In the close vicinity of 9.20 GHz the indices of refraction are obtained to be high, +18 and -12

due to the flatness of EFS contours around 9.20 GHz [Fig. 8(c)]. The refractive indices are negative in the frequency range 9.25–10.00 GHz. As seen in Fig. 11 the refractive indices depend strongly on the frequency. This is an expected behavior since the EFCs [Fig. 8(c)] are anisotropic throughout the frequency range of interest. Measured refractive index values are -0.65 , -0.85 , -0.88 , and -0.96 for four different incidence angles of 15° , 25° , 35° , and 45° , respectively at 9.70 GHz. These results indicate that the refractive index depends on the incidence-angle which renders the medium highly anisotropic. This anisotropy and its consequences on the characterization of the refractive properties of the PC in terms of an effective refractive index were discussed by Notomi.⁴⁾ To obtain uniform angle-independent negative index of refraction two conditions must be satisfied. First, a circular EFC centered at the origin of the Brillouin zone is required. Second, the radius of circular EFC must be decreasing with increasing frequency.²²⁾

We have also scanned the intensity distribution of the EM wave by a monopole antenna mounted to a 2D scanning table with $\Delta x = \Delta z = 2.5$ mm steps. In our experiments we can only measure the power at a certain point, which corresponds to the time averaged intensity at that point. Note that upto this point we have only scanned the field along PC–air interface for measuring the index of refraction. The resulting scanned field profile at 9.70 GHz is plotted in Fig. 12. We can clearly see how the wave propagates after being refracted from the PC–air interface. The intensities are normalized with respect to the maximum intensity. The incident EM wave has a Gaussian beam profile centered at $x = 0$. Gaussian beam is shifted by 40 mm to the negative side of the normal as expected from a negatively refracting medium.

A similar field scan is performed for the observation of focusing through a PC slab lens. In this case we have used a monopole antenna as a point source to shine the air–PC interface [refer to Fig. 2(b) for setup]. EM waves emerging from a point source located near a lens with negative refractive index will first be refracted through the first air–PC interface and will come into focus inside the PC. Then outgoing EM waves will face refraction again at the second PC–air interface and the refracted beam will meet the optical axis of flat lens, where the second focusing will occur.

Figure 13 provides the transmission spectrum for the omni-directional source located at $d_s = 7$ cm away from the PC lens. Number of layers along the propagation direction is

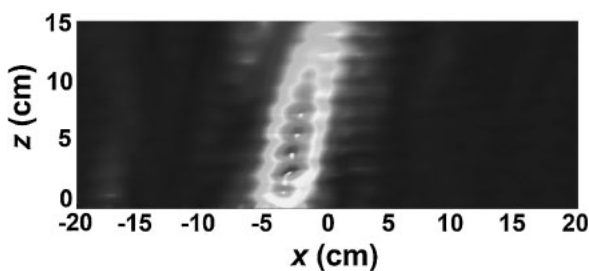


Fig. 12. Spatial intensity distribution of an outgoing EM wave at 3.70 GHz along the x - z plane. The wave is refracted negatively since the beam emerges from the negative side of the normal.

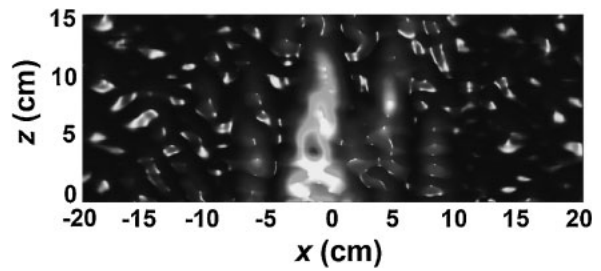


Fig. 13. Spatial intensity distribution of an omni-directional source at 3.70 GHz along the x - z plane. Focusing through a slab of photonic crystal is observed.

$N_z = 10$. As seen in Fig. 13, an image is formed at a focal length of $z = 4$ cm. Focusing is obtained both in the lateral and the propagation direction. If the slab was made of a positive refractive material, it would not be possible to observe a point focusing. For such positive refractive index slab lenses the beam will diverge as expected from ray optics. Therefore flat lens focusing is available only for negative refractive media.

5. Conclusions

In this article, the negative refraction and the focusing abilities of 2D dielectric and metallodielectric photonic crystals are investigated both experimentally and theoretically. We have observed that an effective index of refraction can be defined from the band structure of the PC, which, under convex EFCs, can take negative values and can be associated with refraction of electromagnetic waves through the PC. The isotropy and spectral range of the refractive indices depend strongly on the details of the band structure. The focusing abilities associated with negative refraction is promising since both the subwavelength imaging and far-field focusing are achievable using PC with appropriate band structures. Our studies showed that negative refraction is available both for TM and TE polarized incident electromagnetic waves. Metallodielectric crystals are used to obtain negative refractive indices over a wide range of angles. Dielectric rods are inserted within metallic crystal, resulting band diagram is calculated and a lowering in frequency of the bands is observed.

The advantage of using photonic crystals as negative refractive media is that the transmission is higher compared to lossy left-handed materials. Also the electromagnetic phenomena with discussed here depend only on the refractive index of the dielectric material and on the geometrical parameters of the 2D PC, hence it is scalable across the electromagnetic spectrum. With advancing fabrication techniques, photonic crystals are now envisaged as essential building blocks of applications in the infrared and optical frequencies. It is much more difficult to scale the left-handed materials that are made of metallic structures.

Acknowledgements

This work is supported by the European Union under the projects EU-DALHM, EU-NOE-METAMORPHOSE, EU-NOE-PHOREMOST, and TUBITAK under Project No. 104E090. Ekmel Ozbay acknowledges partial support from the Turkish Academy of Sciences.

- 1) E. Yablonovitch: Phys. Rev. Lett. **58** (1987) 2059.
- 2) S. John: Phys. Rev. Lett. **58** (1987) 2486.
- 3) J. D. Joannopoulos, R. D. Meade and J. N. Winn: *Photonic Crystals: Molding the Flow of Light* (Princeton University Press, Princeton, NJ, 1995).
- 4) M. Notomi: Phys. Rev. B **62** (2000) 10696.
- 5) B. Gralak, S. Enoch and G. Tayeb: J. Opt. Soc. Am. A **17** (2000) 1012.
- 6) C. Luo, S. G. Johnson, J. D. Joannopoulos and J. B. Pendry: Phys. Rev. B **65** (2002) 201104.
- 7) S. Foteinopoulou, E. N. Economou and C. M. Soukoulis: Phys. Rev. Lett. **90** (2003) 107402.
- 8) E. Cubukcu, K. Aydin, E. Ozbay, S. Foteinopoulou and C. M. Soukoulis: Nature **423** (2003) 604.
- 9) P. V. Parimi, W. T. Lu, P. Vodo, J. Sokoloff, J. S. Derov and S. Sridhar: Phys. Rev. Lett. **92** (2004) 127401.
- 10) A. Berrier, M. Mulot, M. Swillo, M. Qiu, L. Thylén, A. Talneau and S. Anand: Phys. Rev. Lett. **93** (2004) 073902.
- 11) H. Kosaka, T. Kawashima, A. Tomita, M. Notomi, T. Tamamura, T. Sato and S. Kawakami: Phys. Rev. B **58** (1998) R10096.
- 12) S. Foteinopoulou and C. M. Soukoulis: Phys. Rev. B **67** (2003) 235107.
- 13) E. Cubukcu, K. Aydin, E. Ozbay, S. Foteinopoulou and C. M. Soukoulis: Phys. Rev. Lett. **91** (2003) 207401.
- 14) P. V. Parimi, W. T. Lu, P. Vodo and S. Sridhar: Nature **426** (2003) 404.
- 15) C. Luo, S. G. Johnson, J. D. Joannopoulos and J. B. Pendry: Phys. Rev. B **68** (2003) 045115.
- 16) C. Luo, S. G. Johnson, J. D. Joannopoulos and J. B. Pendry: Opt. Express **11** (2003) 746.
- 17) S. Foteinopoulou and C. M. Soukoulis: Phys. Rev. B **72** (2005) 165112.
- 18) R. Moussa, S. Foteinopoulou, L. Zhang, G. Tuttle, K. Guven, E. Ozbay and C. M. Soukoulis: Phys. Rev. B **71** (2005) 085106.
- 19) K. Guven, K. Aydin, K. B. Alici, C. M. Soukoulis and E. Ozbay: Phys. Rev. B **70** (2004) 205125.
- 20) E. Ozbay, K. Guven, E. Cubukcu, K. Aydin and B. K. Alici: Mod. Phys. Lett. B **18** (2004) 1275.
- 21) A. Martínez, H. Míguez, A. Griol and J. Martí: Phys. Rev. B **69** (2004) 165119.
- 22) I. Bulu, H. Caglayan and E. Ozbay: Phys. Rev. B **72** (2005) 045125.
- 23) P. Vodo, P. V. Parimi, W. T. Lu, S. Sridhar and R. Wing: Appl. Phys. Lett. **85** (2005) 1858.
- 24) P. Vodo, P. V. Parimi, W. T. Lu and S. Sridhar: Appl. Phys. Lett. **86** (2005) 201108.
- 25) V. G. Veselago: Sov. Phys. Usp. **10** (1968) 504.
- 26) D. R. Smith, W. J. Padilla, D. C. Vier, S. C. Nemat-Nasser and S. Schultz: Phys. Rev. Lett. **84** (2000) 4184.
- 27) J. B. Pendry: Phys. Rev. Lett. **85** (2000) 3966.
- 28) Koray Aydin, K. Guven, M. Kafesaki, L. Zhang, C. M. Soukoulis and E. Ozbay: Opt. Lett. **29** (2004) 2623.
- 29) R. A. Shelby, D. R. Smith and S. Schultz: Science **292** (2001) 77.
- 30) Koray Aydin, K. Guven, C. M. Soukoulis and E. Ozbay: Appl. Phys. Lett. **86** (2005) 124102.
- 31) C. Monzon, P. Loschialpo, D. Smith, F. Rachford, P. Moore and D. W. Forester: Phys. Rev. Lett. **96** (2006) 207402.
- 32) B. Temelkuran, E. Ozbay, J. P. Kavanaugh, G. Tuttle and K. M. Ho: Appl. Phys. Lett. **72** (1998) 2376.
- 33) P. V. Parimi, W. T. Lu, P. Vodo and S. Sridhar: Nature **426** (2003) 404.
- 34) E. Ozbay, G. Tuttle, R. Biswas, K. M. Ho, J. Bostak and D. M. Bloom: Appl. Phys. Lett. **65** (1994) 1617.
- 35) W. T. Lu and S. Sridhar: Opt. Express **13** (2005) 10673.
- 36) M. Bayindir, S. Tanriseven and E. Ozbay: Appl. Phys. A **72** (2001) 117.
- 37) R. Gajic, R. Meisels, F. Kuchar and K. Hingerl: Phys. Rev. B **73** (2006) 165310.
- 38) M. Bayindir and E. Ozbay: Phys. Rev. B **62** (2000) R2247.
- 39) A. Locatelli, M. Conforti, D. Modotto and C. D. Angelis: Opt. Lett. **31** (2006) 1343.
- 40) E. Ozbay and B. Temelkuran: Appl. Phys. Lett. **69** (1996) 743.
- 41) S. Foteinopoulou and C. M. Soukoulis: Phys. Rev. B **72** (2005) 165112.
- 42) M. Kafesaki, C. M. Soukoulis and M. Agio: J. Appl. Phys. **96** (2004) 4033.
- 43) E. Ozbay, M. Bayindir, I. Bulu and E. Cubukcu: IEEE J. Quantum Electron. **38** (2002) 837.